The Astrophysical Journal, 962:58 (16pp), 2024 February 10 https://doi.org/10.3847/1538-4357/ad18b4

Properties of Voids and Void Galaxies in the `TNG300` Simulation

Olivia Curtis, Bryanne McDonough, and Tereasa G. Brainerd
Department of Astronomy & Institute for Astrophysical Research, 725 Commonwealth Ave., Boston University, Boston, MA 02215, USA

Received 2023 September 29; revised 2023 December 5; accepted 2023 December 24; published 2024 February 7

Abstract

We investigate the properties of voids and void galaxies in the `TNG300` simulation. Using a luminous galaxy catalog and a spherical void-finding algorithm, we identify 5078 voids at redshift $z = 0$. The voids cover 83% of the simulation volume and have a median radius of 4.4 h^{-1} Mpc. We identify two populations of field galaxies based on whether the galaxies reside within a void ("void galaxies"; 75,220 objects) or outside a void ("nonvoid galaxies"; 527,454 objects). Within the voids, mass does not directly trace light. Instead, the mean radial underdensity profile as defined by the locations of void galaxies is systematically lower than the mean radial underdensity profile as defined by the dark matter (i.e., the voids are more "devoid" of galaxies than they are of mass). Within the voids, the integrated underdensity profiles of the dark matter and the galaxies are independent of the local background density (i.e., voids-in-voids versus voids-in-clouds). Beyond the void radii, however, the integrated underdensity profiles of both the dark matter and the galaxies exhibit strong dependencies on the local background density. Compared to nonvoid galaxies, void galaxies are on average younger, less massive, bluer in color, less metal enriched, and have smaller radii. In addition, the specific star formation rates of void galaxies are ~20% higher than nonvoid galaxies and, in the case of galaxies with central supermassive black holes with $M_{\rm BH} \gtrsim 3 \times 10^6\, h^{-1}\, M_\odot$, the fraction of active void galaxies is ~25% higher than active nonvoid galaxies.

Unified Astronomy Thesaurus concepts: Large-scale structure of the universe (902); Voids (1779); Magnetohydrodynamical simulations (1966); Galaxy evolution (594)

1. Introduction

The large-scale structure of the Universe is an interconnected network of walls, sheets, filaments, and galaxy clusters, between which lie vast regions of near nothingness known as cosmic voids (see, e.g., Giovanelli & Haynes 1991). The origin of the "cosmic web" dates back to the early Universe during the epoch of inflation, when quantum fluctuations near the end of the inflationary period gave rise to slight anisotropies in the post-inflation matter density field. These anisotropies are observed in the cosmic microwave background (CMB), with regions that deviate by a few microkelvin from the average CMB temperature (see, e.g., Planck Collaboration et al. 2020), and they are responsible for the structure that is seen in the cosmic web today.

Perturbations in the density field are unstable. Regions that are overdense experience an inward gravitational force, causing them to increase in density as they collapse and accrete surrounding matter (Bertschinger 1998). The opposite is true for regions that are initially underdense. Matter in these regions experiences an outward gravitational force that attracts it toward nearby, higher-density regions. As matter streams out, these regions become more underdense, increasing the relative outward gravitational pull and causing them to expand even further. Since these expanding regions never become virialized, their growth can always be modeled by linear perturbation theory (see, e.g., Goldberg & Vogeley 2004). Primordial overdensities in the post-inflation matter density field evolved in a bottom-up, hierarchical fashion consistent with cold dark matter (CDM) theory (see, e.g., Liddle & Lyth 1993), forming halos, clusters, walls, and filaments. Conversely, primordial underdensities expanded, becoming the voids.

Voids have properties that make them interesting regions for performing various cosmological tests (Sheth & van de Weygaert 2004), and the interiors of mature voids can be described as low-density Friedmann–Lemaître–Robertson–Walker universes (see, e.g., Icke 1984; van de Weygaert & van Kampen 1993). This makes voids excellent laboratories for tests of the expansion rate and geometry of the Universe, the dark energy equation of state, and modified theories of gravity (see, e.g., Li et al. 2012; Clampitt et al. 2013; Gibbons et al. 2014; Cai et al. 2015; Pollina et al. 2016; Cai et al. 2017; Falck et al. 2018; Paillas et al. 2019). Furthermore, since voids are smaller than the mean-free path of neutrinos (Lesgourgues & Pastor 2006), voids can be used to constrain the sum of neutrino masses via tests that examine the ways in which neutrino properties affect the sizes and distributions of voids (see, e.g., Villaescusa-Navarro et al. 2013; Massara et al. 2015; Banerjee & Dalal 2016; Kreisch et al. 2019; Schuster et al. 2019; Contarini et al. 2021).

Voids are not completely devoid of internal structure, and even the most mature voids in the local Universe show substructure in the form of galaxies and diffuse filaments (Szomoru et al. 1996; El-Ad & Piran 1997; Hoyle & Vogeley 2004; Sheth & van de Weygaert 2004; Kreckel et al. 2012; Alpaslan et al. 2014). The dynamical structure within voids can have significant impact on cosmic flow patterns in the local Universe, with matter around the ridges of voids affecting the peculiar motions of galaxies around nearby walls and filaments (see, e.g., Bothun et al. 1992; van de Weygaert 2016; Vallés-Pérez et al. 2021; Bermejo et al. 2022).

Additionally, the fact that voids resemble low-density universes with large Hubble parameters (see, e.g., Icke 1984; Goldberg & Vogeley 2004) makes void galaxies interesting objects with which to test models of galaxy formation and evolution. From linear theory, it is known that dark matter halos in underdense regions of the Universe form later in the history of the Universe than do their counterparts in overdense regions (Liddle & Lyth 1993). Therefore, studying the physical properties of void galaxies in the local Universe has the potential to provide insight into an early epoch of galaxy evolution.

Furthermore, the degree to which the location of a galaxy within the cosmic web affects the evolution of the galaxy is an open question. Some studies have concluded that, due to their differing dynamical histories, void galaxies differ systematically from nonvoid field galaxies (see, e.g., Peebles 2001; Croton et al. 2005; Kreckel et al. 2012; Rodríguez Medrano et al. 2022; Rosas-Guevara et al. 2022). For example, when compared to observed galaxies in walls and filaments, some studies have found that void galaxies are, on average, bluer in color, have lower stellar masses, are richer in H I, have higher specific star formation rates, and have later morphological types (see, e.g., Rojas et al. 2004; Croton et al. 2005; Hoyle et al. 2012; Kreckel et al. 2012; Beygu et al. 2016; Douglass et al. 2018; Florez et al. 2021; Pandey et al. 2021; Rodríguez Medrano et al. 2022). However, other studies have found little to no difference between the stellar masses, gas content, star formation rates, chemical abundances, dark matter profiles, or metallicities of void versus nonvoid field galaxies (see, e.g., Szomoru et al. 1996; Patiri et al. 2006; Moorman et al. 2014; Liu et al. 2015; Douglass & Vogeley 2017; Douglass et al. 2019; Wegner et al. 2019; Domínguez-Gómez et al. 2022).

The properties of void and nonvoid galaxies have also been studied in recent magnetohydrodynamical (MHD) simulations of Lambda cold dark matter (ΛCDM) universes. In agreement with some observational studies, Rosas-Guevara et al. (2022) found that, compared to galaxies in denser environments, void galaxies in the `EAGLE` simulation (Schaye et al. 2015) have lower stellar mass fractions. In addition, Rosas-Guevara et al. (2022) found clear trends of galaxy properties as a function of the distances of galaxies from the nearest void center. In particular, star formation activity and H I gas density decreased with increasing void-centric distance, and stellar mass fraction increased with increasing void-centric distance. Similarly, in a study of galaxies in the `HorizonAGN` simulation (Dubois et al. 2016), Habouzit et al. (2020) found that low-stellar-mass galaxies with high star formation rates occur more frequently in the inner regions of voids than in denser regions of the cosmic web.

Another open question involves the degree to which the location of a galaxy within the cosmic web influences the formation of active galactic nuclei (AGNs). Some studies have concluded that the AGN fraction of galaxies is independent of the local matter density (e.g., Karhunen et al. 2014; Sabater et al. 2015; Amiri et al. 2019; Habouzit et al. 2020), while others have found a positive correlation with local matter density (e.g., Manzer & De Robertis 2014; Argudo-Fernández et al. 2018). Still other studies have concluded that there is a negative correlation between AGN fraction and the local matter density (e.g., Kauffmann et al. 2004; Constantin et al. 2008; Platen 2009; Lopes et al. 2017; Mishra et al. 2021; Ceccarelli et al. 2022).

The relatively isolated nature of void galaxies suggests that their growth and evolution do not depend strongly on merger-driven nuclear activity. For example, Ceccarelli et al. (2022) found that the growth channels for void galaxies and their central, supermassive black holes (SMBHs) differed from those of their nonvoid counterparts. Ceccarelli et al. (2022) attribute this to the fact that, compared to the SMBHs in their nonvoid galaxies, the SMBHs in their void galaxies had larger surrounding O III reservoirs that fed into the central regions of the galaxies. In contrast, however, Habouzit et al. (2020) found that void galaxies and their SMBHs in the `HorizonAGN` simulation grow in a manner that is similar to that of galaxies in denser environments, where merger-driven nuclear activity is common. Understanding the discrepancies between these results could further our understanding of the various ways in which nuclear activity is triggered, as well as the effects that cosmic flow patterns and mergers have on AGNs.

Here, we investigate the properties of voids and void galaxies in the $z = 0$ snapshot of the `TNG300` simulation (hereafter `TNG300`; Marinacci et al. 2018; Naiman et al. 2018; Nelson et al. 2018; Pillepich et al. 2018; Springel et al. 2018). `TNG300` is a cosmological MHD simulation of a ΛCDM universe with sufficient spatial and mass resolution within a large volume to conduct statistical analyses of voids and void galaxies. Using `TNG300`, we construct the largest catalog of luminous void galaxies within a cosmological MHD simulation to date. We compare various physical properties (sizes, colors, star formation rates, luminosity functions, mass functions, metallicities, and nuclear activity) of the void galaxies to those of galaxies found in walls and filaments. In addition, we examine the degree to which location within the cosmic web (i.e., within voids and outside voids) affects AGN activity.

This paper is organized as follows. `TNG300` and our void-finding algorithm are discussed in Section 2. In Section 3, we present the properties of the voids and the void galaxies, and we compare the properties of void galaxies to nonvoid field galaxies. A summary and discussion of our results is presented in Section 4. Throughout, we compute error bars using 10,000 bootstrap resamplings of the data. Error bars are omitted from figures when the error bars are comparable to or smaller than the sizes of the data points.

2. Methodology

2.1. `TNG300`

We use the $z = 0$ snapshot of the highest-resolution `TNG300` simulation to obtain our sample of galaxies and voids. `TNG300` is the largest simulation box in the IllustrisTNG suite of simulations (Marinacci et al. 2018; Naiman et al. 2018; Nelson et al. 2018; Pillepich et al. 2018; Springel et al. 2018), encompassing a comoving volume of $205^3\ h^{-3}$ Mpc^3. A total of 2500^3 dark matter particles of mass $m_{\rm dm} = 4.0 \times 10^7\ h^{-1}\ M_\odot$ and 2500^3 hydrodynamical gas cells with initial baryonic mass $m_{\rm b} = 7.5 \times 10^6\ h^{-1}\ M_\odot$ were used. In the $z = 0$ snapshot, the gravitational force softening is $1.0\ h^{-1}$ kpc and the smallest hydrodynamical gas cells are $125\ h^{-1}$ pc in extent. The volume of the simulation is sufficient for the identification of voids with radii as large as $\sim 25\ h^{-1}$ Mpc, and the spatial and mass resolution of the simulation is sufficient for the identification of galaxies with stellar masses as small as $10^7\ h^{-1}\ M_\odot$. The cosmological parameters adopted in the simulation are $\Omega_{\Lambda,0} = 0.6911$, $\Omega_{m,0} = 0.3089$, $\Omega_{b,0} = 0.0486$, $\sigma_8 = 0.8159$, $n_s = 0.9667$, and $h = 0.6774$ (e.g., Planck Collaboration et al. 2016).

To identify luminous galaxies, we use the publicly available `TNG300` subhalo and group catalogs, which list friends-of-friends groups and their substructures. Excluding subhalos that are flagged as being noncosmological in origin, there are a total of 664,322 luminous galaxies. To assign luminosities to the galaxies, we adopt the subhalo magnitudes from the supplementary catalog created by Nelson et al. (2018). In comparison to the main IllustrisTNG subhalo catalog, the Nelson et al. (2018) catalog better resembles Sloan Digital Sky Survey (SDSS; York et al. 2000) photometry because it includes the effects of dust obscuration on the simulated galaxies.

In addition to the group and subhalo catalogs, we also make use of particle data from the $z = 0$ snapshot, including stellar, dark matter, gas, and black hole particles. Following Pillepich et al. (2018), when quoting stellar masses for our `TNG300` galaxies we apply a 40% correction to the stellar masses from the `TNG300` catalog (i.e., to account for the fact that the stellar masses in `TNG300` are not as well converged as in the benchmark TNG100 simulation; see Appendix A of Pillepich et al. 2018).

2.2. Void Finder

To identify voids, we use the 3D spherical void finder (SVF) from Padilla et al. (2005) as implemented by Paillas et al. (2017) and Paillas et al. (2019).[1] This is a computationally inexpensive algorithm that identifies regions with significant central underdensities that converge to the average density beyond the ridges of the voids at $\gtrsim 3$ void radii. The SVF algorithm can be summarized as follows:

1. A rectangular grid is constructed over the galaxy distribution. The number of galaxies within each cell is then counted and any cell that is completely devoid of galaxies (i.e., the cell contains no galaxies) is considered to be a void center.
2. Spheres are expanded outwards from each void center. The largest sphere around a void center with an integrated underdensity contrast $\Delta_{\rm void} \leqslant -0.8$ has its radius defined to be the radius of the void. The choice of setting the underdensity contrast threshold to -0.8 comes from linear theory arguments in Blumenthal et al. (1992), who showed that voids at the present epoch should have interior densities that are 20% of the mean density of the Universe at the time of shell crossing.
3. Any void that neighbors a larger void by more than 20% of the sum of the radii of both voids is rejected. That is, if the distance, d, between voids i and j (where radius $R_i \leqslant R_j$) satisfies $d \leqslant 0.2^*(R_i + R_j)$, void i is rejected from the sample.
4. Remaining voids have their centers perturbed in random directions to determine whether their radii can be increased. If a shifted void center results in a larger sphere that satisfies the underdensity contrast criterion from Step 2, the center and radius of the void are then updated to the values of the larger sphere.

The rectangular grid from Step 1 contains cells that are $5\,h^{-1}$ Mpc on a side. The grid size was chosen as a balance between (i) computation time, (ii) reducing the error associated with the locations of the centers of the smallest voids, and (iii) reducing the number of spurious centers (which can arise due to shot noise). That is, if a void center is identified with low resolution, the error associated with the radius of that void will be adversely affected (i.e., since the radius depends on the integrated underdensity contrast threshold in the region surrounding that center). Therefore, a cell size is chosen such that the error it contributes to the radius of the smallest voids in our sample is less than 10% of the total error for that result (see Paillas et al. 2017 for a detailed discussion).

The 3D SVF does not provide the detailed description of void geometry that can be obtained with more sophisticated void-finding algorithms (see, e.g., Platen et al. 2007; Neyrinck 2008); however, voids in the local Universe tend to exhibit spherical symmetry (see, e.g., Icke 1984; Sheth & van de Weygaert 2004; Sutter et al. 2014; Hamaus et al. 2016). Moreover, Paillas et al. (2019) compared the results of six void-finding techniques in the context of differentiating $f(R)$ gravity models and found that similar results were obtained regardless of the choice of void-finding algorithm. For our purposes, then, we consider the 3D SVF to be a reasonable choice of algorithm.

2.3. Field Galaxy Sample

Our investigation of galaxy properties focuses on field galaxies (i.e., galaxies that reside outside cluster environments), subdivided according to whether the galaxies reside within a void ("void galaxies") or outside a void ("nonvoid galaxies"). We define field galaxies to be all galaxies that are not contained within parent halos with masses $\geqslant 10^{14}\,h^{-1}\,M_\odot$, which eliminates cluster galaxies from the sample. We then use the void catalog from Section 2.2 to separate void galaxies from nonvoid galaxies. From this, our field galaxy sample consists of 75,220 void galaxies and 527,454 nonvoid galaxies.

As part of our analysis, we investigate the relative ages of void and nonvoid galaxies. Even in simulation space, determining the formation time of a galaxy is not simple. This is due to the hierarchical nature of structure formation, which results in many smaller overdensities merging to form a single galaxy. Here, we adopt two indicators of galaxy age: (i) the age of the oldest bound stellar particle, and (ii) the luminosity-weighted age. For both of these age indicators, we use the subhalo cutout provided by the `TNG`, which contains all particles that are identified by the `SUBFIND` algorithm as being bound to the halo. The formation times of stellar particles are given as scale factors in the simulation, and we convert these to lookback times using the Planck Collaboration et al. (2016) cosmological parameters and the `astropy.cosmology` package (Astropy Collaboration et al. 2013, 2018).

The age of the oldest bound stellar particle is a useful indicator of the age of a simulated galaxy, but it is not straightforward to use as a comparison to observed galaxies. In contrast, the luminosity-weighted age is a metric that can be compared to observations (see, e.g., Li et al. 2018). To obtain luminosity-weighted ages of the simulated galaxies, we use the following equation from Lu et al. (2020):

$$\langle x \rangle = \frac{\sum_{k=1}^{N} L_k x_k}{\sum_{k=1}^{N} L_k}, \tag{1}$$

where x_k is the logarithm (base 10) of the formation age of the kth particle and L_k is the SDSS r-band luminosity of the kth particle. Above, the summation is computed over all stellar particles that are bound to the subhalo.

---

[1] https://github.com/epaillas/voidfinder/

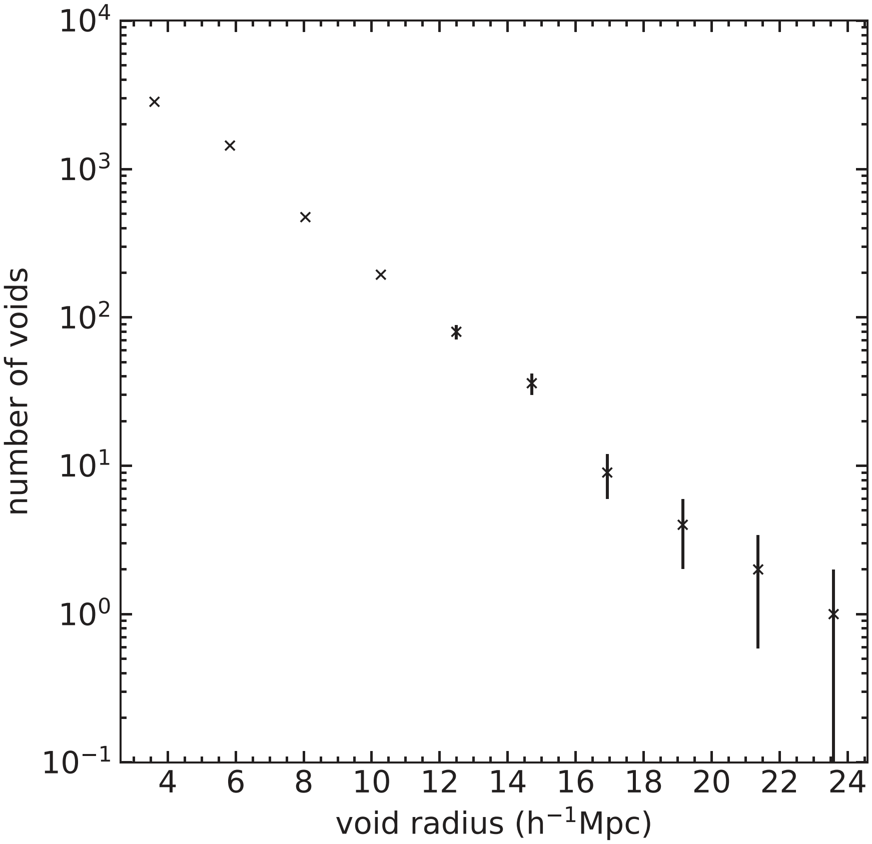

Figure 1. Distribution of void radii.

3. Results

3.1. Void Properties

Using the 3D SVF algorithm, a total of 5078 voids were identified. The void radii span an order of magnitude, with the smallest voids having radii of $r_v = 2.5\,h^{-1}$ Mpc and the largest void having a radius of $r_v = 24.7\,h^{-1}$ Mpc. The median void radius is $4.4\,h^{-1}$ Mpc. In total, voids cover a volume of $168.3^3 h^{-3}$ Mpc^3, or 82% of the simulation box. The number of voids as a function of radius is shown in Figure 1, from which it is clear that the majority of voids have radii $\lesssim 10\,h^{-1}$ Mpc.

The mean radial number density contrast of the voids is shown in Figure 2. Squares show the result obtained using the luminous galaxies ("luminous density contrast") and crosses show the result obtained using the dark matter particles ("dark matter density contrast"). For each void, the density contrast in concentric spherical shells of thickness δr, centered on the void center, was calculated as

$$\Delta = \frac{n(r)}{\bar{n}(r)} - 1, \tag{2}$$

where $n(r)$ is the number of galaxies or dark matter particles within the radial bin that ranges from $r - \frac{\delta r}{2}$ to $r + \frac{\delta r}{2}$, and $\bar{n}(r)$ is the average number density of galaxies or dark matter particles within the simulation box. In both cases (i.e., luminous density contrast and dark matter density contrast), the mean radial density profiles resemble reverse spherical top-hat distributions, which are expected for underdense regions in the local Universe (see, e.g., Icke 1984; Sheth & van de Weygaert 2004). These profiles are characterized by an underdense, flat interior that rises steeply above the mean density at the ridge of a void and slowly decreases to the mean density at large distances from the void center.

From Figure 2, it is clear that mass does not directly trace light within the voids. Rather, the mean central density contrast obtained from the galaxies ($\Delta = -0.77 \pm 0.04$) is somewhat lower than the mean central density contrast of the dark matter ($\Delta = -0.64 \pm 0.02$), i.e., the centers of the voids are more "devoid" of galaxies than they are of dark matter. The opposite is true at the ridges of the voids where, on average, there is a higher concentration of galaxies than dark matter, with the mean dark matter density contrast reaching a maximum of 0.33 ± 0.02 at $r = 1.25 r_v$ and the mean luminous density contrast reaching a maximum contrast of 0.42 ± 0.02 at $r = 1.4 r_v$.

Voids form in regions of space with differing background densities (i.e., as compared to the average density of the Universe). That is, some voids form in regions of space that have relatively high local background densities ("voids in clouds"), while others form in regions of space that have relatively low local background densities ("voids in voids"); see Sheth & van de Weygaert (2004) for a discussion of void hierarchy. In Figure 3, we use mean integrated number density profiles to explore the effects of the local background density on the density contrast. For legibility of the figure, the number density profiles for the dark matter particles are shown as spline fits. Following Sheth & van de Weygaert (2004), we define voids-in-voids to be those with an integrated galaxy density contrast <0 at $r = 3 r_v$ and voids-in-clouds to be those with an integrated galaxy density contrast >0 at $r = 3 r_v$. To construct the mean integrated density profiles, the number density

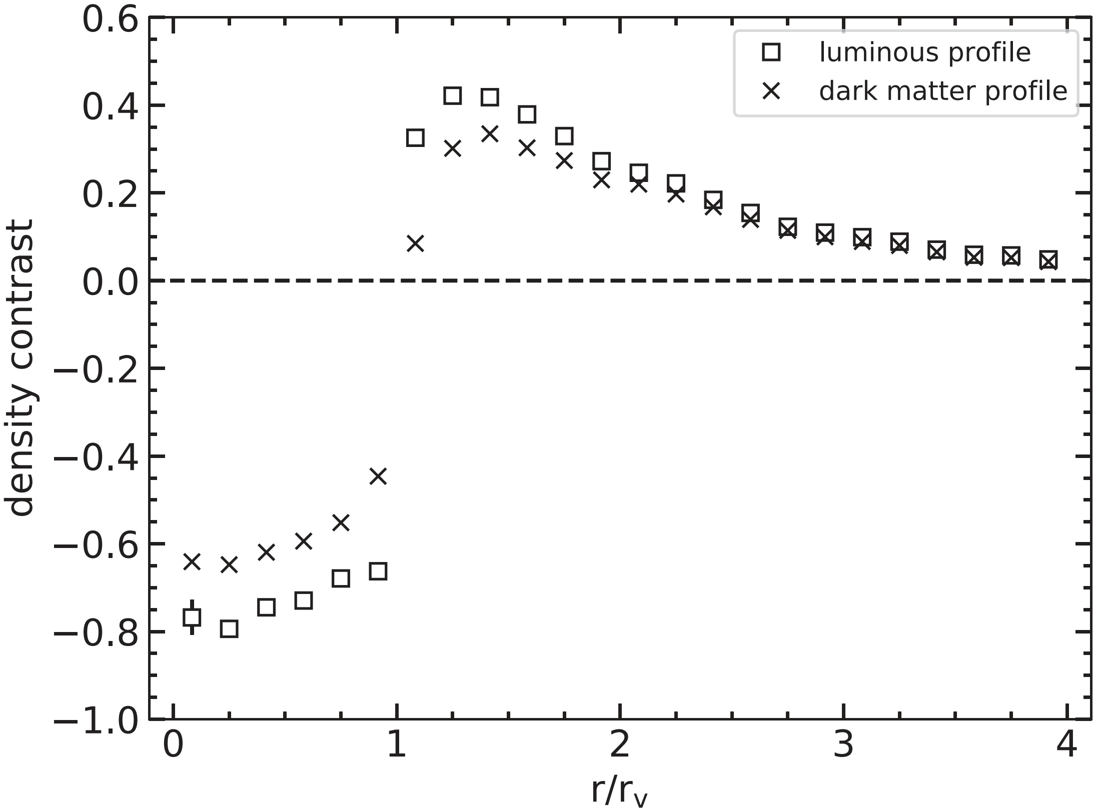

Figure 2. Average radial number density contrast profiles for the voids, computed using concentric spherical shells centered on the void centers. Radii of the shells are given in units of the void radius, r_v. Squares: number density contrast of the luminous galaxies. Crosses: number density contrast of the dark matter particles.

contrast of the galaxies (points) and the dark matter particles (lines) was computed in concentric spheres of radius r, centered on each void center, from which means were then computed.

The mean integrated number density profiles obtained using all voids (blue line and blue circles in Figure 3) show the same trends as the mean differential number density profiles in Figure 2. On average, the central regions of the voids have a dark matter density contrast that is 65% ± 2% lower than the average dark matter density contrast in the simulation and a galaxy density contrast that is 77% ± 4% lower than the average galaxy density contrast in the simulation. At the ridges of the voids, the mean interior density contrast for the galaxies reaches a maximum that is 22% ± 1% higher than the average galaxy density contrast at $r = 2.08r_v$ and the mean interior density contrast for the dark matter reaches a maximum that is 18% ± 2% higher than the average dark matter density contrast at $r = 2.25r_v$.

For radii $r \lesssim r_v$, the local background density in which the voids are located has relatively little effect on the integrated number density profiles of the galaxies and the dark matter. For radii $r > r_v$, however, significant differences for the integrated number density profiles of voids-in-voids (black line and green diamonds) and voids-in-clouds (yellow line and red crosses) occur. In the case of voids-in-voids, galaxies largely trace the dark matter for $r \gtrsim r_v$. At the ridges of voids-in-voids, the mean interior density contrast remains less than the average in the simulation (i.e., the mean interior density contrast is -0.20 ± 0.01 at the ridges) and for radii $1.5r_v \lesssim r \lesssim 4r_v$ the mean interior density contrast of voids-in-voids remains approximately constant at a value of ~ -0.2. In the case of voids-in-clouds, the galaxies trace the dark matter for a small range of radii ($r_v \lesssim r \lesssim 1.2r_v$), but are more overdense than the dark matter for $r \gtrsim 1.2r_v$. At the ridges of voids-in-clouds, the integrated number densities of the galaxies and dark matter exceed the integrated number densities of the galaxies and dark matter in the full void sample by a factor of ∼3 and they remain significantly higher than than the average density out to distances as large as $\sim 4r_v$.

3.2. Properties of Void and Nonvoid Galaxies

Below, we investigate the following properties of void and nonvoid galaxies: (i) the distribution of physical sizes, (ii) optical color–magnitude relationships, (iii) luminosity and stellar mass functions, (iv) ages, (v) stellar and gas chemical abundances, (vi) specific star formation rates, and (vii) relationships between stellar mass and SMBH mass, as well as AGN fraction.

3.2.1. Physical Sizes

The `TNG300` subhalo catalog defines the photometric radii of the galaxies to be the radii at which the surface-brightness profiles drop below 20.7 mag arcsec^{-1} in the K band. We use this definition to compute normalized probability distributions for the radii of void and nonvoid galaxies, the results of which are shown in Figure 4. From this figure, the majority of the galaxies in both populations have radii $\lesssim 5\, h^{-1}$ kpc, and the probability of a given galaxy having a radius $\lesssim 5\, h^{-1}$ kpc is the same for both void and nonvoid galaxies. For galaxy radii $\gtrsim 5\, h^{-1}$ kpc, the distribution of void galaxy radii declines much more steeply than the distribution of nonvoid galaxy radii. As a result, the largest void galaxies have radii $\sim 11\, h^{-1}$ kpc, while the largest nonvoid galaxies have radii that are ∼2 times larger than the largest void galaxies.

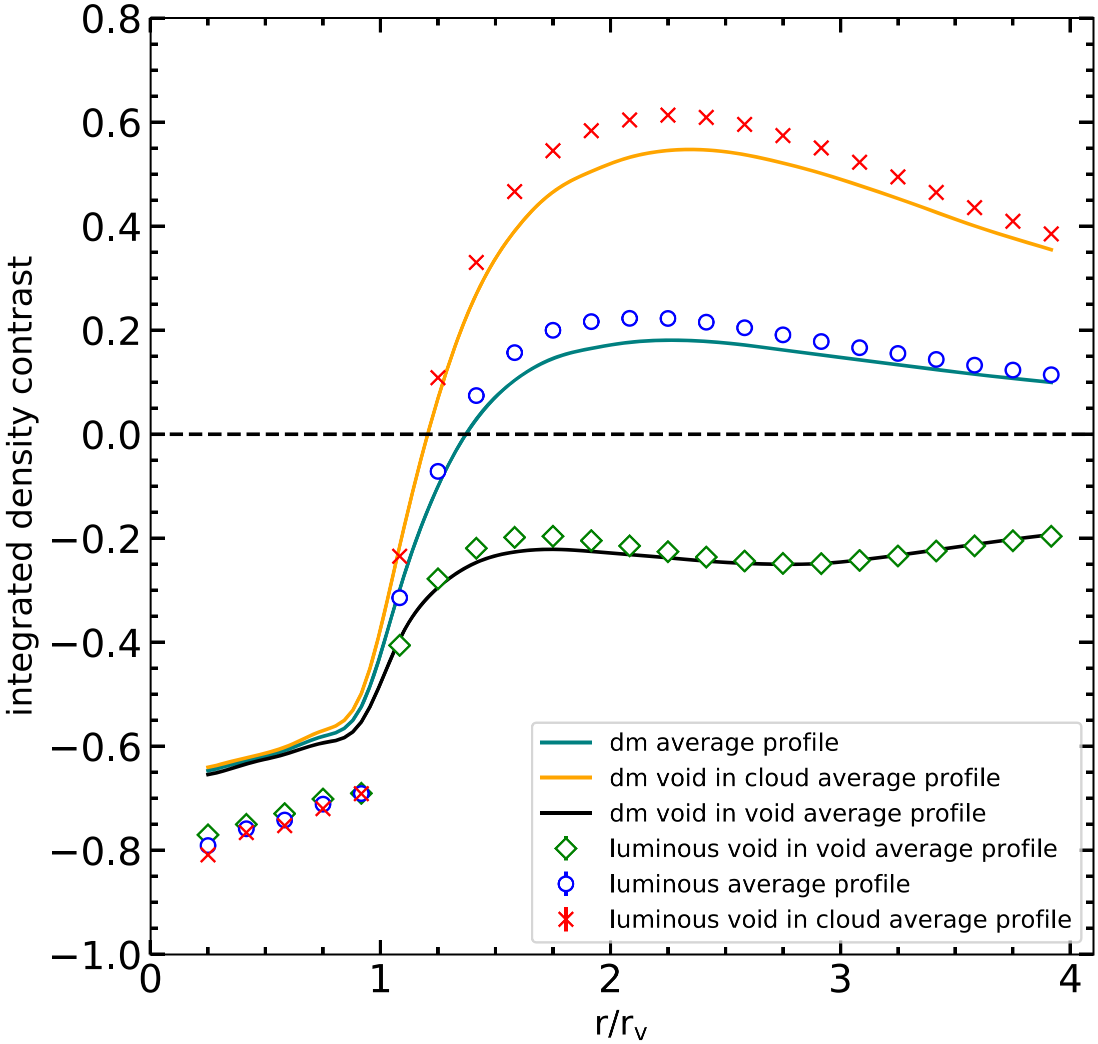

Figure 3. Mean integrated number density contrast computed using luminous galaxies (points) and dark matter particles (lines). Blue line and blue circles: results obtained using all voids in the simulation. Yellow line and red crosses: results for voids in regions of the simulation that have a high local background density ("voids-in-clouds"). Black line and green diamonds: results for voids in regions of the simulation that have a low local background density ("voids-in-voids"). See text for definitions of voids-in-clouds and voids-in-voids.

3.2.2. Optical Color–Magnitude Relationships

Figure 5 shows the relationship between the $(g - r)$ optical color and the absolute SDSS r-band magnitude, M_r, for nonvoid galaxies (panel b) and void galaxies (panel d). From these, it is clear that both void and nonvoid galaxies have distributions that peak in two locations: (i) intrinsically bright, red galaxies, and (ii) intrinsically faint, blue galaxies. Red crosses in panels (b) and (d) of Figure 5 indicate the locations of the peaks, and show that the peaks occur in similar locations of the $(g - r)$ versus M_r space for both void and nonvoid galaxies. Formally, the blue peak occurs at $(M_r,\ g - r) = (-14.77,\ 0.59)$ for the void galaxies and at $(M_r,\ g - r) = (-14.76,\ 0.64)$ for the nonvoid galaxies, i.e., the blue peaks occur at identical absolute magnitudes but slightly different colors, with the void galaxies being somewhat bluer than the nonvoid galaxies near the blue peaks. The red peak occurs at $(M_r,\ g - r) = (-20.47,\ 0.77)$ for the void galaxies and at $(M_r,\ g - r) = (-20.55,\ 0.77)$ for the nonvoid galaxies, i.e., the red peaks occur at essentially identical absolute magnitudes and colors for both populations of galaxies.

Panels (a) and (c) in Figure 5 show normalized probability distributions for the absolute r-band magnitudes of the nonvoid and void galaxies, respectively. From this, it is clear that the distributions differ signficantly, and this will be reflected in the luminosity functions of void and nonvoid galaxies below. Panel (e) in Figure 5 shows normalized probability distributions for the $(g - r)$ colors of void galaxies (diamonds) and nonvoid galaxies (circles). From this, it is clear that, while both types of galaxies have a broad distribution of optical colors, the distributions are substantially different and, in particular, there is a much higher concentration of red, nonvoid galaxies than red, void galaxies.

We further explore the differences between the optical color distributions for void and nonvoid galaxies in Figure 6, which shows the cumulative probability distributions of $(g - r)$ values for void galaxies (diamonds) and nonvoid galaxies (circles). A two-sample Kolmogorov–Smirnov (KS) test performed on the two distributions in Figure 6 rejects the null hypothesis that both distributions are drawn from the same underlying distribution at a high confidence level (>99.9999%), indicating that the distribution of void galaxy colors is significantly

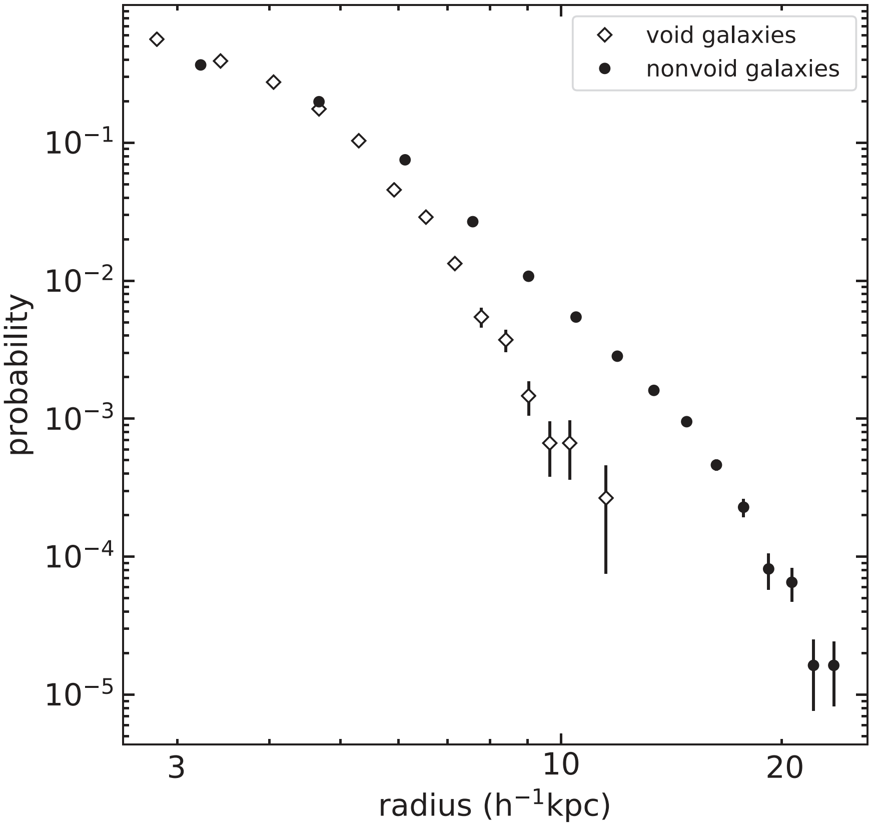

Figure 4. Probability distributions for the radii of void galaxies (diamonds) and nonvoid galaxies (circles).

different from that of nonvoid galaxies. In particular, void galaxies are typically bluer than nonvoid galaxies, with the median $(g - r)$ color of void galaxies being 0.4205 ± 0.0007 and the median $(g - r)$ color of nonvoid galaxies being 0.4881 ± 0.0003.

3.2.3. Luminosity and Stellar Mass Functions

Next, we compute luminosity functions and stellar mass functions for void and nonvoid galaxies. Figure 7 shows the luminosity functions, computed in terms of SDSS r-band absolute magnitude (i.e., the number of galaxies per magnitude per unit volume). Lines in Figure 7 show the best-fitting Schechter luminosity functions (Schechter 1976) of the form

$$\Phi(M)dM = 0.4\ln(10)\ \Phi_*\,[10^{0.4(M_*-M)}]^{(1+\alpha)} \times \exp[-10^{0.4(M_*-M)}]dM, \quad (3)$$

where M_* is the absolute magnitude of an L_* galaxy.

Overall, the luminosity functions of both void and nonvoid galaxies are fitted reasonably well by Schechter functions, though some deviation is apparent (particularly at the extreme ends of the luminosity functions). The parameters of the best-fitting Schechter functions are $\phi_* = (1.9 \pm 0.2) \times 10^{-3}$ Mpc^{-3}, $M_* = -20.5 \pm 0.1$ and $\alpha = -1.17 \pm 0.03$ (nonvoid galaxies), and $\phi_* = (1.7 \pm 0.2) \times 10^{-3}$ Mpc^{-3}, $M_* = -21.1 \pm 0.1$ and $\alpha = -1.11 \pm 0.02$ (void galaxies). Within the formal errors, the luminosity functions have characteristic bright galaxy absolute magnitudes, M_*, that differ significantly, i.e., $L_{*,r}$ nonvoid galaxies are intrinsically ∼70% brighter than $L_{*,r}$ void galaxies. However, the faint-end slopes of the luminosity functions, α, are consistent within 2σ.

Results for the differential stellar mass functions (i.e., the number of galaxies per log stellar mass bin per unit volume) of void and nonvoid galaxies are shown in Figure 8. For stellar masses between $10^{7.25}\,h^{-1}\,M_\odot$ and $10^{10.25}\,h^{-1}\,M_\odot$, the mass functions exhibit roughly power-law behaviors, with the slope of the power law being substantially shallower for nonvoid galaxies than it is for void galaxies. Below stellar masses of $10^{7.25}\,h^{-1}\,M_\odot$, both mass functions fall below the power law due to the finite resolution of the simulation, which leads to undercounting of the smallest galaxies. Above stellar masses of $10^{10.25}\,h^{-1}\,M_\odot$, both mass functions decrease sharply due to the fact that high-mass galaxies are relatively rare objects. From the high-mass ends of the mass functions, however, it is clear that the sample of nonvoid galaxies has a larger fraction of high-mass galaxies than does the void galaxy sample. The combined differences in the mass functions result in the median stellar mass for the void galaxies being a factor of ∼2 smaller than the median stellar mass for the nonvoid galaxies: $(1.58 \pm 0.01) \times 10^8\,h^{-1}\,M_\odot$ versus $(3.08 \pm 0.01) \times 10^8\,h^{-1}\,M_\odot$.

3.2.4. Ages

Next, we quantify the ages of the void and nonvoid galaxies using two metrics: (i) the oldest stellar particles within the subhalos, and (ii) the luminosity-weighted ages of the galaxies (see Equation (1)). From this, the median age of the oldest stellar particles bound to the subhalos in the void galaxies is 10.1033 ± 0.0001 Gyr and the median age of the oldest stellar particles bound to the subhalos in the nonvoid galaxies is 10.10685 ± 0.00003 Gyr, i.e., the oldest stellar particles bound to the subhalos in the void galaxies are ∼3.6 Myr years younger than the oldest stellar particles in the nonvoid galaxies.

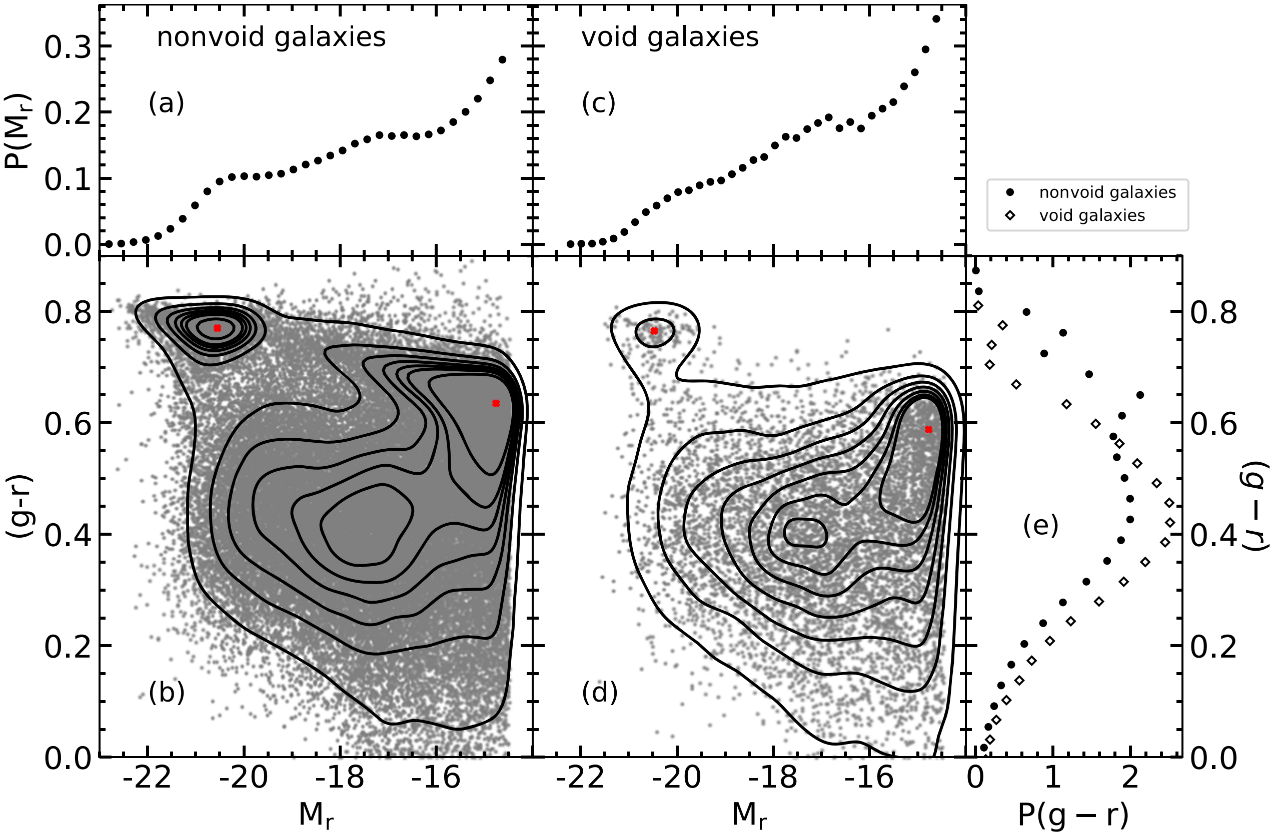

Figure 5. Optical color–magnitude relations for nonvoid galaxies (panel (b)) and void galaxies (panel (d)). Black contours: linearly spaced density contours, computed using all galaxies in each sample. Gray points: 10% of the nonvoid galaxies, randomly selected from the complete sample (panel (b)) and 100% of the void galaxies (panel (d)). Red crosses indicate the red and blue peaks for each of the distributions. Top panels: normalized probability distributions for the r-band absolute magnitudes of nonvoid galaxies (panel (a)) and void galaxies (panel (c)). Side panel: normalized probability distributions of the $(g-r)$ colors of void galaxies (diamonds) and nonvoid galaxies (circles).

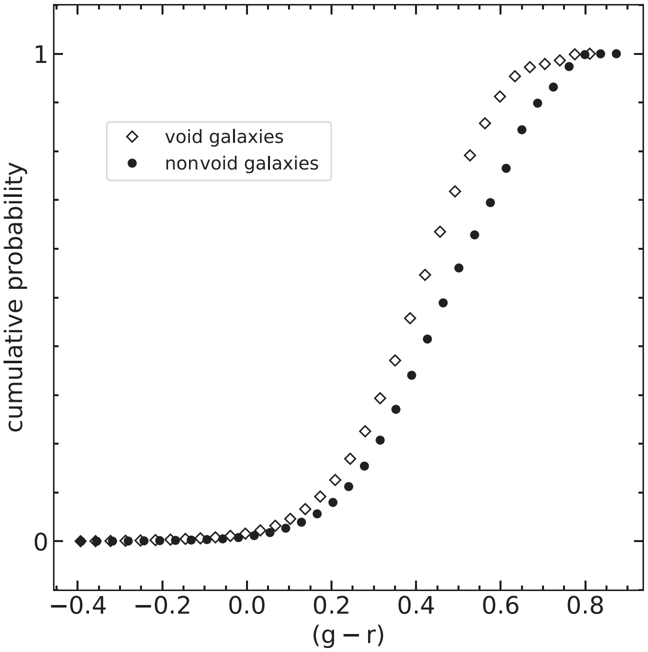

Figure 6. Cumulative probability distribution functions for $(g-r)$ galaxy colors. Diamonds: void galaxies. Circles: nonvoid galaxies.

In comparison, the median luminosity-weighted age of the void galaxies is 9.217 ± 0.002 Gyr and the median luminosity-weighted age of the nonvoid galaxies is 9.3642 ± 0.0009 Gyr, i.e., when using luminosity-weighted ages, we find that the void galaxies are ∼147 Myr younger than the nonvoid galaxies. Both age indicators reveal that void galaxies are systematically younger than nonvoid galaxies, but the age difference between void and nonvoid galaxies is reflected less by the time at which the first stars formed (i.e., the ages of the oldest stellar particles) than it is by the overall star formation histories of the galaxies (i.e., the luminosity-weighted ages). That being said, the difference between the median luminosity-weighted ages of void and nonvoid galaxies is too small to be detected in modern surveys, which report typical dispersions for luminosity-weighted ages of galaxy populations between 0.15 and 0.30 dex (see, e.g., González Delgado et al. 2014; Scott et al. 2017; Li et al. 2018; Lu et al. 2020).

3.2.5. Stellar and Gas Chemical Abundances

Results for the stellar and gas chemical abundance ratios are shown in Figures 9 and 10, respectively. Here, we subdivide the galaxy samples using four distinct stellar mass bins, the boundaries of which are $M_* = 10^{7.40}\,h^{-1}\,M_\odot$, $10^{8.15}\,h^{-1}\,M_\odot$, $10^{8.90}\,h^{-1}\,M_\odot$, $10^{9.65}\,h^{-1}\,M_\odot$, and $10^{10.40}\,h^{-1}\,M_\odot$. These are indicated by vertical, dashed blue lines in Figure 8. The panels in Figures 9 and 10 are arranged vertically in order of increasing stellar mass, such that panels (a) and (e) include only galaxies in the first bin, panels (b) and (f) include only galaxies in the second bin, panels (c) and (g) include only galaxies in the third bin, and panels (d) and (h) include only galaxies in the fourth bin. The left panels of Figures 9 and 10 show the

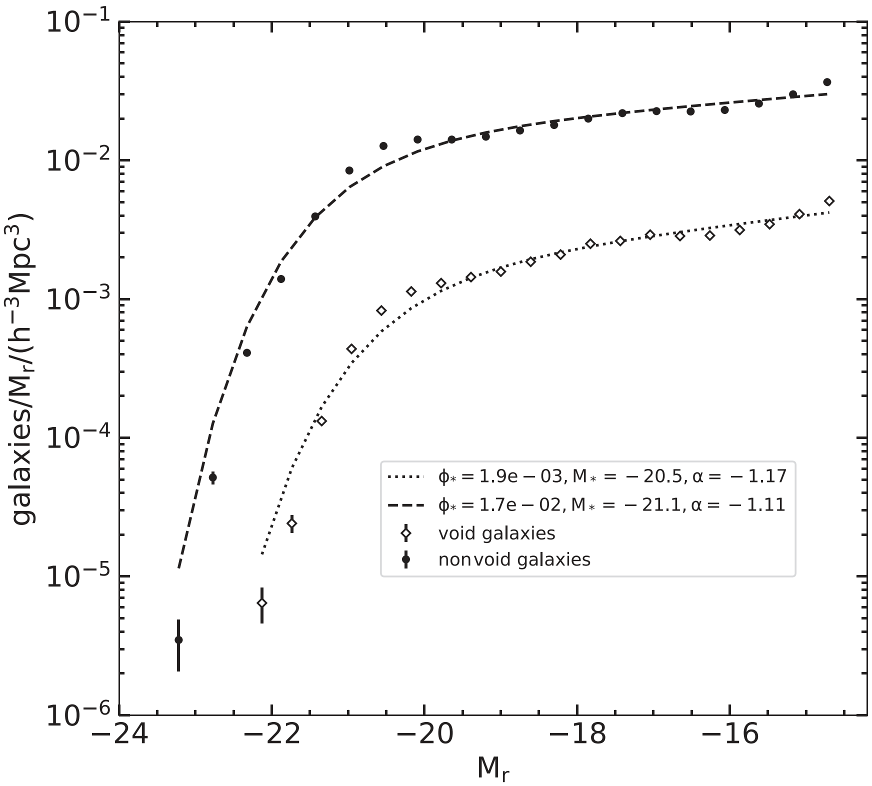

Figure 7. Luminosity functions in the SDSS *r* band for void galaxies (diamonds) and nonvoid galaxies (circles). Dotted line: best-fitting Schechter luminosity function for void galaxies. Dashed line: best-fitting Schechter luminosity function for nonvoid galaxies.

average stellar and gas chemical abundance ratios, respectively. The right panels of Figures 9 and 10 show the ratios of the corresponding data points for void and nonvoid galaxies from the left panels.

From Figures 9 and 10, void galaxies have stellar and gas metal fractions that are systematically lower than those of nonvoid galaxies. This result holds true across all stellar mass bins, but the differences are more pronounced for galaxies with lower stellar masses than they are for galaxies with higher stellar masses. That is, in order of increasing stellar mass, the stellar metallicities of nonvoid galaxies exceed those of void galaxies by ∼20% (Figure 9(e)), ∼8% (Figure 9(f)), ∼6.5% (Figure 9(g)), and ∼2.5% (Figure 9(h)). A similar, but less pronounced, trend is shown by the gas metallicities, i.e., in order of increasing stellar mass, the gas metallicities of nonvoid galaxies exceed those of void galaxies by ∼7.5% (Figure 10(e)), ∼4.5% (Figures 10(f) and (g)), and ∼2% (Figure 10(h)).

3.2.6. Specific Star Formation Rates

Results for the relationships between stellar mass and specific star formation rate (sSFR) are shown in Figure 11(b) (nonvoid galaxies) and Figure 11(c) (void galaxies). Here, the sSFRs are instantaneous rates, derived from the sum of star formation rates in individual gas cells at $z = 0$. From Figures 11(b) and (c), it is clear that both void and nonvoid galaxies show a main sequence of star formation. Normalized 1D probability distributions for M_* and sSFR are also shown in Figure 11 (top panels and side panel, respectively). Red crosses at (8.38, −9.45) in Figure 11(b) and (8.25, −9.40) in Figure 11(d) indicate the peak densities, which were determined from the relative maxima in the top and side panels.

Figure 12 shows the normalized cumulative probability distribution functions for the sSFR of void and nonvoid galaxies. A two-sample KS test shows that the two distributions are not drawn from the same underlying distribution (confidence level >99.9999%). The median sSFR for void galaxies is $21.8\% \pm 0.5\%$ higher than it is for nonvoid galaxies ($5.015^{+0.021}_{-0.018} \times 10^{-10}\ \mathrm{yr}^{-1}$ versus $4.116^{+0.008}_{-0.008} \times 10^{-10}\ \mathrm{yr}^{-1}$); hence, per unit stellar mass, the void galaxies have star formation rates that are higher than those of the nonvoid galaxies.

3.2.7. Supermassive Black Holes and Fraction of Active Galactic Nuclei

Finally, we investigate the relationships between stellar mass and SMBH mass for `TNG300` void and nonvoid galaxies, the results of which are shown in Figure 13 (black points). SMBHs are "seeded" into `TNG` subhalos once the subhalos pass a given mass threshold, and this seeding of SBMHs gives rise to unphysical artifacts in the stellar mass–SMBH mass relationship for SMBH with masses below $\sim 3 \times 10^6\, h^{-1}\, M_\odot$ (i.e., due to recently seeded SMBHs having nearly identical masses, independent of the stellar mass of their host galaxy). Therefore, we focus our analysis below on galaxies for which the masses of the SMBHs are $\gtrsim 3 \times 10^6\, h^{-1}\, M_\odot$, which results in a sample of 107,527 nonvoid galaxies and 10,231 void galaxies. We further subdivide these particular galaxies according to whether or not their SMBHs are in an active state. To do this, we use the ratio of Bondi accretion rate to Eddington accretion rate as a measure of nuclear activity. Following Weinberger et al. (2017), we classify galaxies with ratios greater than 0.05 as "active." From this classification, we find 1330 void galaxies with SMBH masses $\gtrsim 3 \times 10^6\, h^{-1}\, M_\odot$ are in an active state (i.e., an AGN fraction of $13.0\% \pm 0.4\%$) and 11,269 nonvoid

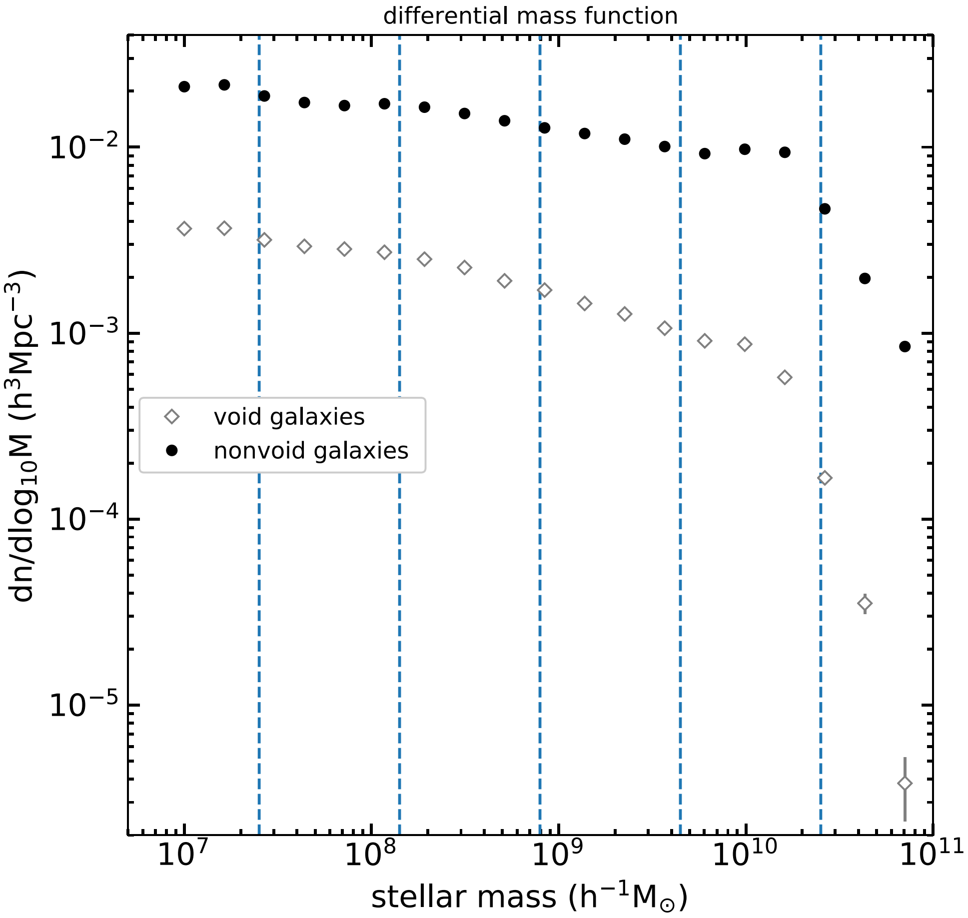

Figure 8. Differential stellar mass functions for void galaxies (diamonds) and nonvoid galaxies (circles). Dashed lines indicate the boundaries of the stellar mass bins used in the analysis of stellar and gas metallicities (see text).

galaxies with SMBH masses $\gtrsim 3 \times 10^6\, h^{-1}\, M_\odot$ are in an active state (i.e., an AGN fraction of $10.5\% \pm 0.1\%$). That is, for `TNG300` galaxies with SMBHs in the mass range that we consider, void galaxies have a somewhat higher ($24\% \pm 4\%$) AGN fraction than do nonvoid galaxies. We also note that it is primarily intermediate-mass SMBHs that are in an active state, since there are few `TNG300` AGNs with SMBH masses $\gtrsim 10^8\, h^{-1}\, M_\odot$ or $\lesssim 10^{6.3}\, h^{-1}\, M_\odot$.

The top panels in Figure 13 show the relationships for galaxies with an inactive SMBH, while the bottom panels show the relationships for galaxies with an active SMBH. Results for nonvoid galaxies are shown in the left panels of Figure 13, and results for void galaxies are shown in the right panels. The observed relationships between stellar mass and SMBH mass from Reines & Volonteri (2015) are also shown in Figure 13 for comparison (red stars, inactive SMBH; green crosses, active SMBH). Observational results for galaxies with an inactive SMBH come from a sample of galaxies with dynamical black hole masses (Table 3 of Reines & Volonteri 2015), and observational results for galaxies with an active SMBH come from a sample of broad-line AGNs (Table 1 of Reines & Volonteri 2015).

From Figure 13, the relationship between SMBH mass and stellar mass for `TNG` galaxies with inactive black holes is in rough agreement with the observational results from Reines & Volonteri (2015). For galaxies with inactive black holes that have masses $\gtrsim 10^7\, h^{-1}\, M_\odot$, there is a tighter relationship between SMBH mass and galaxy stellar mass in the `TNG300` galaxies than there is for observed galaxies. In contrast to observed galaxies, there are no `TNG300` nonvoid galaxies with inactive black holes with masses $>2 \times 10^9\, h^{-1}\, M_\odot$ and no `TNG300` void galaxies with inactive black holes with masses $>7 \times 10^8\, h^{-1}\, M_\odot$. In the case of nonvoid galaxies, inactive SMBHs with masses $>2 \times 10^9\, h^{-1}\, M_\odot$ do exist in the `TNG300` simulation, but all of these objects are located within galaxies that reside in large clusters of galaxies (and all of which were omitted from our sample since the focus of our investigation is the field galaxy population).

Similar to the galaxies with inactive SMBHs, `TNG300` galaxies with active black holes show a much tighter relationship between stellar mass and SMBH mass than do the observed galaxies from Reines & Volonteri (2015). However, while the slope of the relationship is similar to that of observed galaxies with AGNs, the amplitude of the relationship for `TNG300` galaxies with AGNs is significantly higher than it is for observed galaxies. As a result, at fixed stellar mass, the SMBHs in `TNG300` active galaxies are a factor of ∼10 more massive than would be expected based on the best-fitting relationship from Reines & Volonteri (2015; i.e., red dashed lines in Figure 13).

4. Summary and Discussion

Here, we have investigated the properties of voids and void galaxies in the $z = 0$ snapshot of the cosmological MHD simulation `TNG300`. The large volume and high spatial

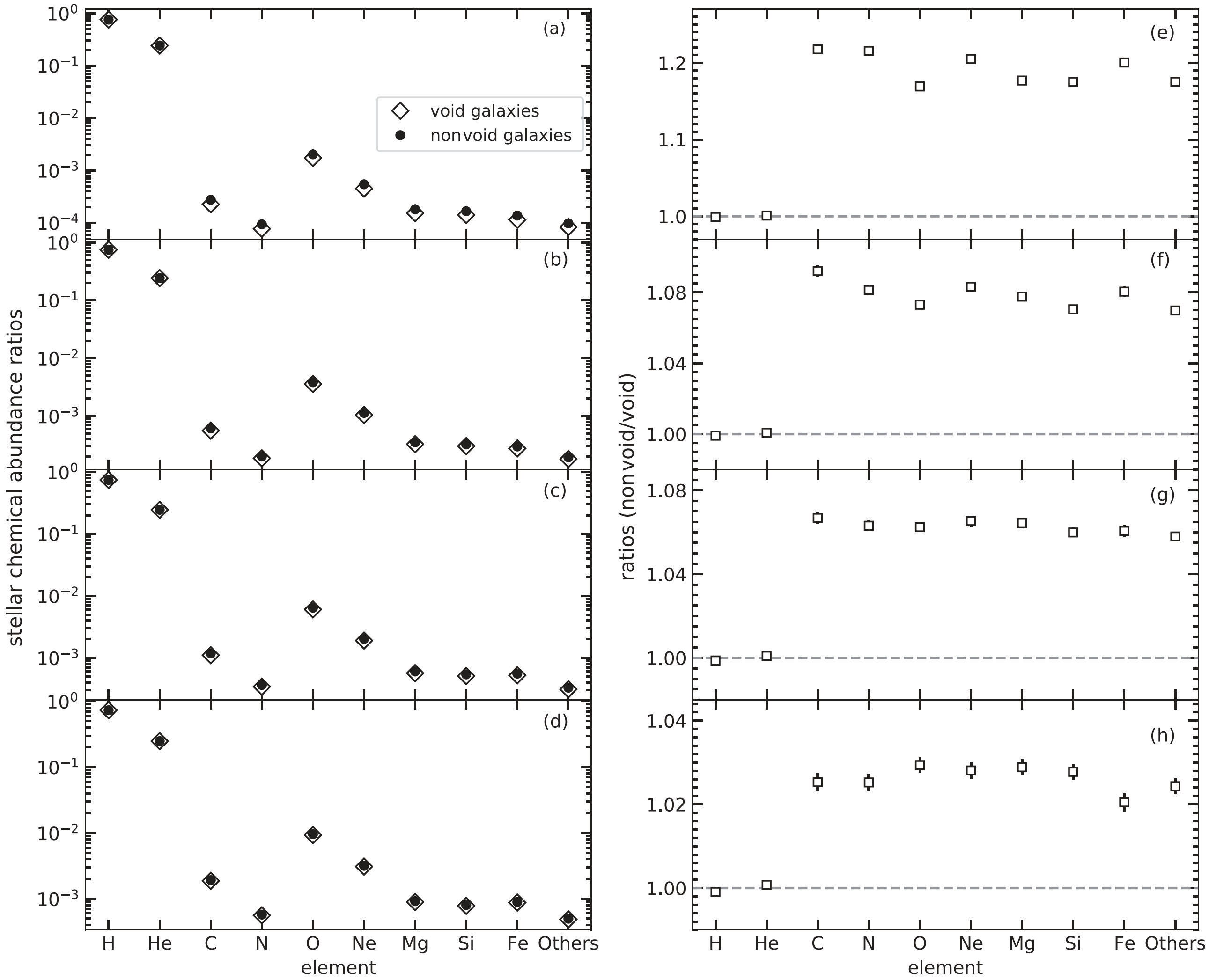

Figure 9. Left: average stellar chemical abundance ratios for void galaxies (diamonds) and nonvoid galaxies (circles). Right: ratios of nonvoid and void galaxy stellar chemical abundances from the left panels. Galaxies with stellar masses $10^{7.40}\,h^{-1}\,M_\odot \leqslant M_* < 10^{8.15}\,h^{-1}\,M_\odot$: panels (a) and (e). Galaxies with stellar masses $10^{8.15}\,h^{-1}\,M_\odot \leqslant M_* < 10^{8.90}\,h^{-1}\,M_\odot$: panels (b) and (f). Galaxies with stellar masses $10^{8.90}\,h^{-1}\,M_\odot \leqslant M_* < 10^{9.65}\,h^{-1}\,M_\odot$: panels (c) and (g). Galaxies with stellar masses $10^{9.65}\,h^{-1}\,M_\odot \leqslant M_* < 10^{10.40}\,h^{-1}\,M_\odot$: panels (d) and (h). Note that, for clarity, different ordinate ranges are used in the right panels.

resolution of `TNG300` makes it possible to study a substantial number of voids and void galaxies.

Voids were identified using a spherical void-finding algorithm that was applied to the `TNG300` galaxy catalog (i.e., in analogy to observational studies of voids and void galaxies, here the voids were identified via underdensities in the distribution of luminous galaxies, not the distribution of dark matter mass or dark matter halos). From this, a total 5078 voids with radii that range from 2.5 h^{-1} Mpc to 24.7 h^{-1} Mpc were identified. The median radius of the `TNG300` voids is 4.4 h^{-1} Mpc, in good agreement with the typical sizes of voids that have been found in `TNG300` (Dávila-Kurbán et al. 2023) and in previous simulations that have computational volumes similar to that of `TNG300` (see, e.g., Paillas et al. 2017; Habouzit et al. 2020).

As expected (see, e.g., Sheth & van de Weygaert 2004), the radial underdensity profiles of the `TNG300` voids follow a reverse spherical top-hat profile. This is the case whether luminous tracers of the underdensity (i.e., luminous galaxies) or dark matter particles are used to compute the profiles.

Recently, Schuster et al. (2023) performed an in-depth study of void profiles in the `Magneticum` suite of cosmological MHD simulations (see, e.g., Dolag et al. 2016 and Hirschmann et al. 2014 for other studies that have used `Magneticum`).[2] The authors find the density profiles of isolated voids to be similar for various void sizes, spatial resolutions, and mass scales. Their stacked, isolated, dark matter void profiles are similar to ours, although our dark matter profile (see Figure 2) has a flatter interior out to $r = r_v$. However, since we do not investigate void profiles as functions of void shape or size, it is difficult to make direct comparisons. Regardless, the similarities to our galaxy number density profile corroborate their conclusion that the physical properties of voids are universal characteristics that are independent of tracer type and resolution.

Dávila-Kurbán et al. (2023) obtained integrated galaxy number density profiles for “voids-in-clouds” and “voids-in-voids” (“S-type” and “R-type” voids in their notation) in `TNG300`. To obtain their void catalog, Dávila-Kurbán et al. (2023) used the void-finding algorithm of Ruiz et al. (2015), a modified version of the void-finding algorithm that we employed, but with a few differences. Dávila-Kurbán et al.

---

[2] http://www.magneticum.org/

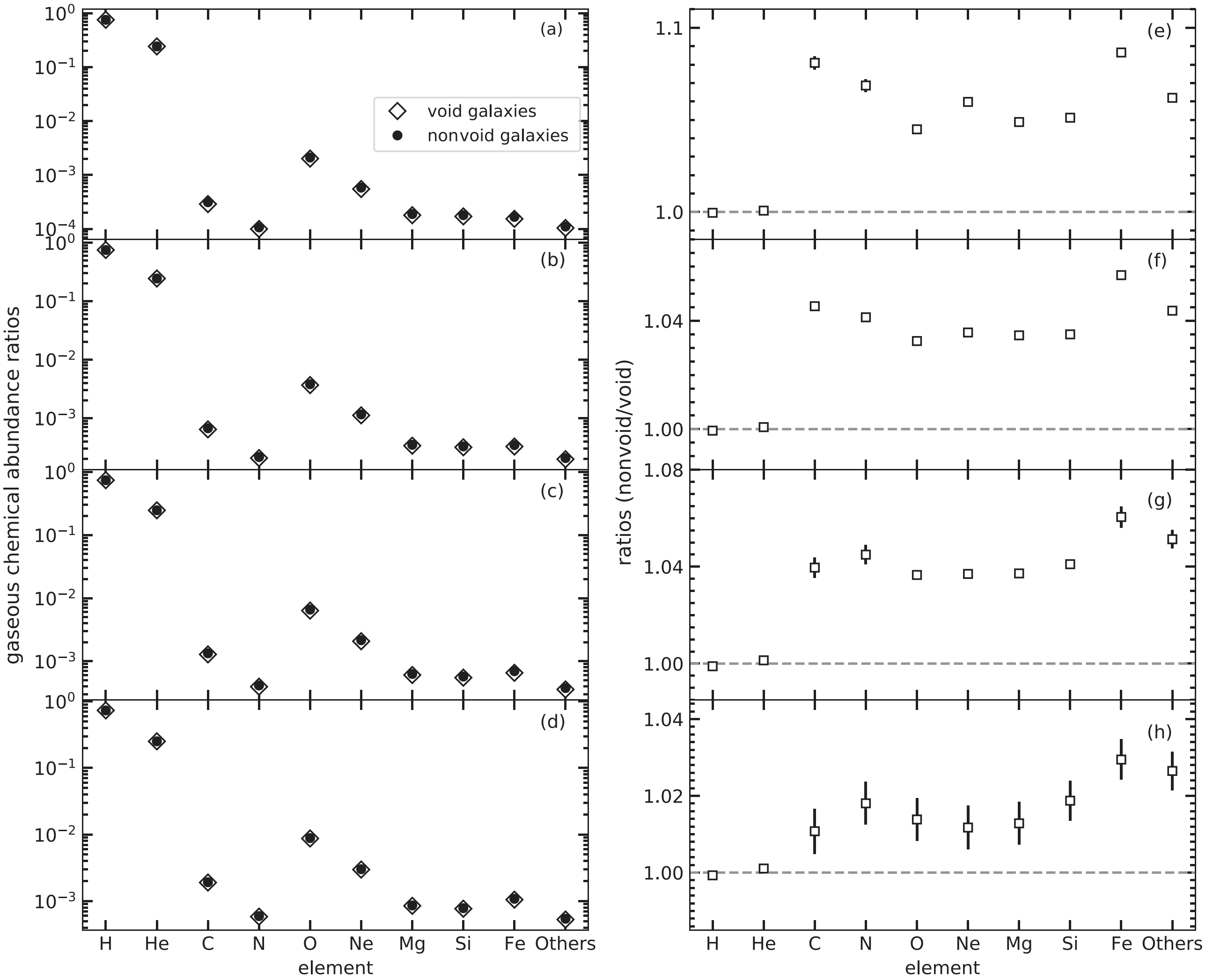

Figure 10. Same as Figure 9, but for chemical abundance ratios of the gas.

(2023) considered candidate void centers as Voronoi cells constructed in the subhalo field that had density contrasts < -0.8; Dávila-Kurbán et al. (2023) also adopted a stricter integrated underdensity contrast threshold of $\Delta_{\rm void} \leqslant -0.9$ for their candidate voids. In addition, Dávila-Kurbán et al. (2023) did not allow for any overlap between voids; instead, they rejected all spheres that overlapped already established, larger voids. Because of this, Dávila-Kurbán et al. (2023) identify far fewer voids in `TNG300` than we do here (82 voids versus 5078 voids), and the radii of their voids are restricted to a much narrower range than the radii of the voids in this work (7–11 h^{-1} Mpc versus 2.5–24.7 h^{-1} Mpc). Because of the differences in void-finding algorithms and size ranges of the resulting voids, we would expect some differences between our results and those of Dávila-Kurbán et al. (2023); and, indeed, this is the case when we compare the two catalogs of "voids-in-clouds." In particular, the ridges of profiles for "voids-in-clouds" in Dávila-Kurbán et al. (2023) only reach maxima up to ~0.3, which is considerably lower than the maximum for our median profile (i.e., 0.6). However, the profiles of "voids-in-voids" in Dávila-Kurbán et al. (2023) are similar to the luminous profiles that we find for our "voids-in-voids."

In the observed Universe, Sánchez et al. (2017) provide 2D photometric galaxy number density profiles for voids in the Dark Energy Survey (DES; Flaugher 2005; Dark Energy Survey Collaboration et al. 2016). These voids were found with a circular void finder, and utilized projected density maps of various thicknesses. Much like our voids, the interiors of DES voids are nearly empty of galaxies. However, the DES voids do not have flat interiors and gradually increase in density out to the ridges of voids. It is unclear whether this is due to projection effects caused by using 2D spectroscopic slices.

Furthermore, several authors have provided void galaxy cross-correlation functions for large voids in various SDSS, SDSS Baryon Oscillation Spectroscopic Survey (BOSS; Dawson et al. 2013), and SDSS extended BOSS (eBOSS; Alam et al. 2021) data releases (see, e.g., Nadathur et al. 2019; Hamaus et al. 2020; Woodfinden et al. 2022). For instance, Nadathur et al. (2019) and Woodfinden et al. (2022) report voids with very empty and flat interiors ($\xi_0 \sim -1.0$) out to around 20 h^{-1} Mpc that reach maxima of $\xi_0 \sim 0.05$ at $\sim 60 R_{\rm v}$. In addition, Hamaus et al. (2020) report values of ξ_0 that rise from ~ -0.90 in the innermost regions to -0.55 by $0.5 R_v$ and 0.2 at $1 R_{\rm v}$. Thus, the innermost regions of our `TNG300` voids appear to have a higher galaxy density than those in the observed Universe, but their profiles rise more gradually out to the effective radii of voids. Despite this, the ridges of `TNG300`

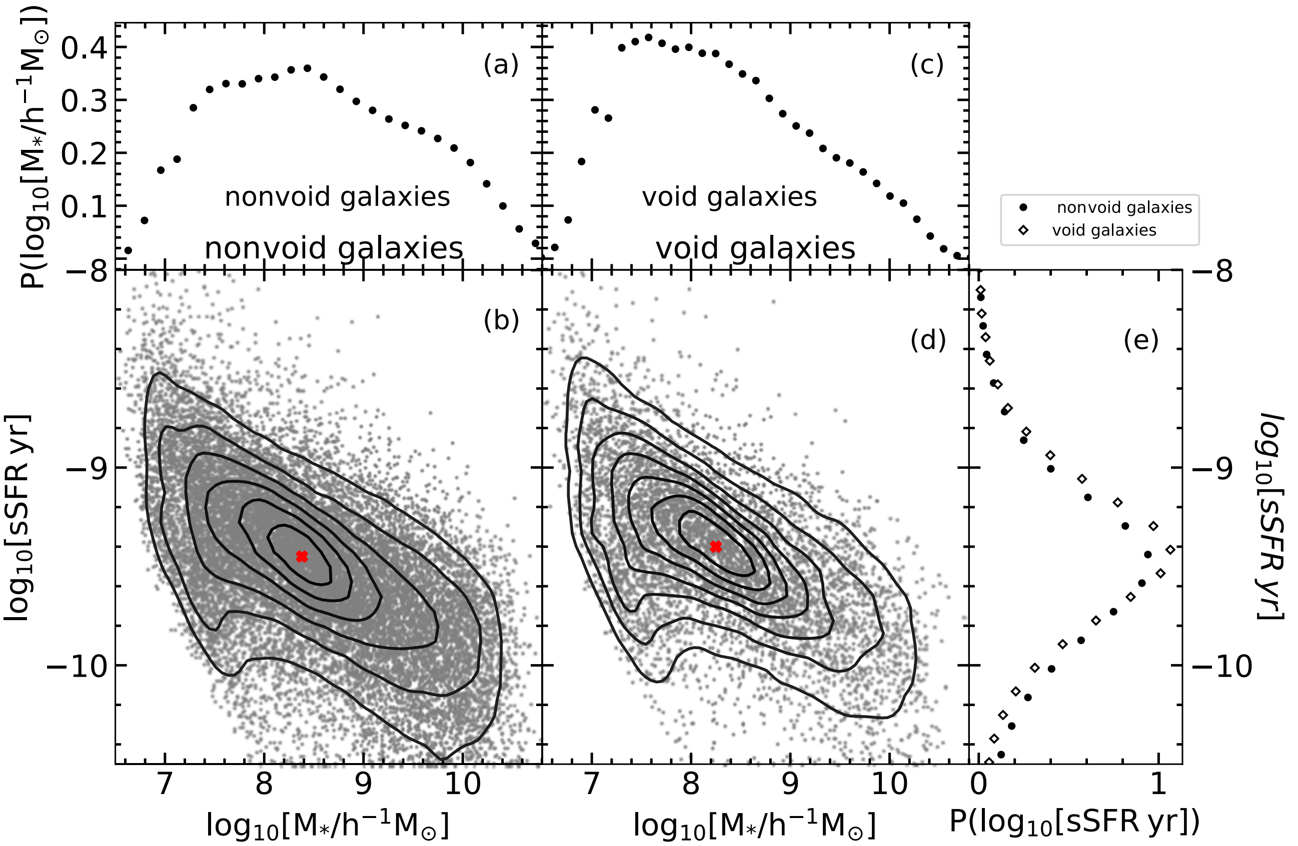

Figure 11. Specific star formation rate vs. stellar mass for nonvoid galaxies (panel (b)) and void galaxies (panel (c)). Black contours: density contours, evenly spaced in the logarithm, computed using all galaxies in each sample. Gray points: 5% of the nonvoid galaxies, randomly selected from the complete sample (panel (b)) and 100% of the void galaxies (panel (d)). Red crosses indicate the central peaks of the distributions. Top: normalized 1D probability distributions for the stellar masses of nonvoid galaxies (panel (a)) and nonvoid galaxies (panel (b)). Side: normalized 1D probability distributions for the sSFR of void galaxies (diamonds) and nonvoid galaxies (circles).

voids have a higher overdensity of galaxies not seen in the observed Universe.

In terms of the detectability of our voids, the small size of most of our voids means their average galaxy number density is orders of magnitudes larger than what is available in most current observational surveys. For instance, we report an average galaxy number density of `TNG300` voids of $9.4 \times 10^{-2}\ h^3\ \mathrm{Mpc}^{-3}$, whereas Mao et al. (2017) found an average galaxy number density of $3.6 \times 10^{-4}\ h^3\ \mathrm{Mpc}^{-3}$ in their SDSS BOSS Data Release 12 void member catalogs. Because of this, it is unlikely that the smaller voids we report would be detected in current-generation surveys.

We find that the `TNG300` voids are more devoid of galaxies than they are of dark matter, and this result is independent of the local background density within which the voids are embedded (i.e., voids-in-voids versus voids-in-clouds). That is, within the voids, mass does not trace light. This result agrees with previous studies that have compared luminous tracers within voids to the underlying dark matter field (see, e.g., Ricciardelli et al. 2014; Pollina et al. 2017). In particular, Pollina et al. (2017) used the `Magneticum` suite to test the linearity of the bias of luminous tracers compared to the underlying dark matter field. There, the authors found a linear relationship between the density contrast of tracers and the density contrast of dark matter within voids when galaxies, clusters, or AGNs are used as tracers.

In addition, we note that previous work on the locations of satellite galaxies in the `Illustris-1` (Vogelsberger et al. 2014a, 2014b; Genel et al. 2014; Sijacki et al. 2015) and TNG100 simulations have demonstrated that mass does not trace light in host-satellite systems (see, e.g., Brainerd 2018; McDonough & Brainerd 2022). Hence, the distribution of luminous galaxies in a ΛCDM universe is an unreliable tracer of the dark matter distribution in overdense regions of space. However, the linear bias between the galaxy and dark matter distributions in underdense regions still makes galaxies valuable probes of the density field within the linear regime of voids.

In `TNG300`, we identified a total of 75,220 void galaxies and 527,454 nonvoid field galaxies, and systematic differences between the void and nonvoid galaxies are clear. Compared to the nonvoid galaxies, the void galaxies are, on average, younger, bluer in color, less metal enriched, have lower stellar masses, and have smaller physical extents. The luminosity functions of both void and nonvoid galaxies exhibit similar faint-end slopes, but the luminosity of an L_* nonvoid galaxy is $\sim$70% greater than the luminosity of an L_* void galaxy, consistent with void galaxies being smaller and less massive than nonvoid galaxies on average. In addition, void galaxies have a somewhat higher sSFR than nonvoid galaxies and, in the case of galaxies with central SMBHs with masses $\gtrsim 3 \times 10^6\ h^{-1}\ M_\odot$, void galaxies have a somewhat higher AGN fraction than nonvoid galaxies. These results are in

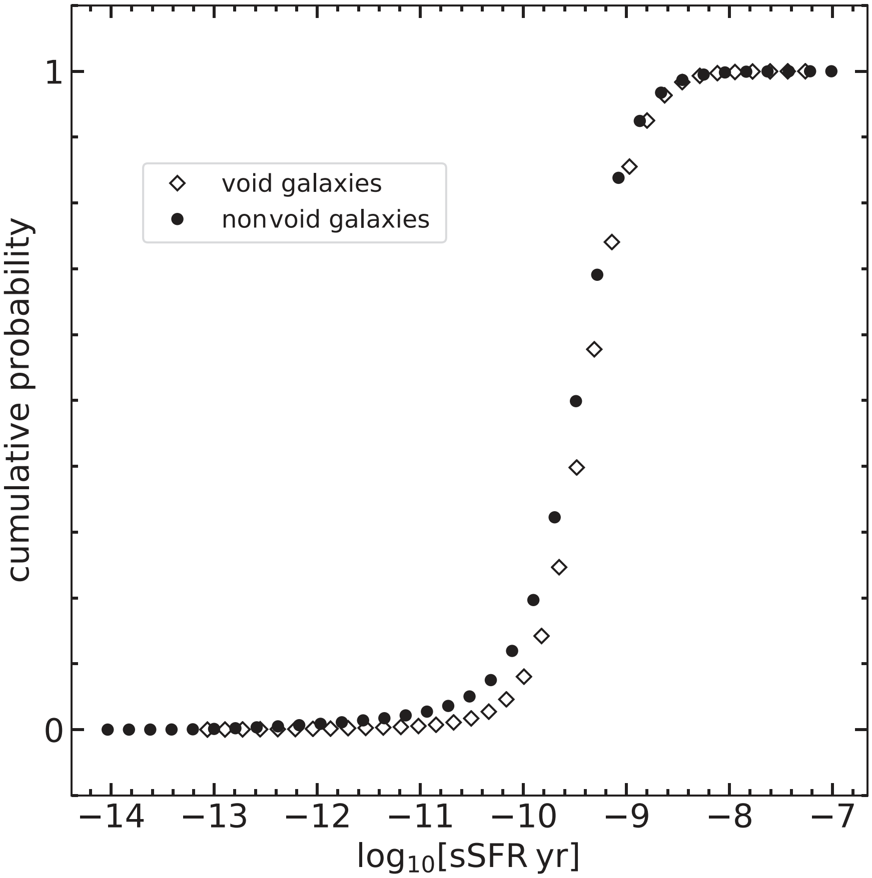

Figure 12. Normalized cumulative probability distribution functions for the specific star formation rates of void galaxies (black diamonds) and nonvoid galaxies (black circles).

agreement with previous studies that find void galaxies to be bluer, lower in stellar mass, and less metal enriched than nonvoid galaxies (see, e.g., Rojas et al. 2004; Florez et al. 2021; Rosas-Guevara et al. 2022) and that concluded AGN fraction is not strongly dependent upon the local matter density of a galaxy (see, e.g., Carter et al. 2001; Karhunen et al. 2014; Habouzit et al. 2020).

The relationship between central SMBH mass and host-galaxy stellar mass was also investigated. In the case of `TNG300` galaxies with inactive SMBHs, the SMBH mass–stellar mass relationships of void and nonvoid galaxies is in rough agreement with results obtained by Reines & Volonteri (2015) for observed galaxies. However, for galaxies with SMBH masses $\gtrsim 10^7\,h^{-1}\,M_\odot$, the SMBH mass–stellar mass relationship is considerably tighter for `TNG300` galaxies than it is for observed galaxies. A relationship between SMBH mass and stellar mass that is tighter for `TNG300` galaxies than observed galaxies is also shown by void and nonvoid `TNG300` galaxies with active central black holes. In both cases, the tightness of the relationship for simulated galaxies may simply be reflective of the relative ease with which both parameters can be obtained in simulation space. Lastly, while the slopes of the SMBH mass–stellar mass relationships for active `TNG300` void and nonvoid galaxies agree well with those of observed galaxies, at fixed stellar mass the SMBHs in active `TNG300` galaxies are ∼10 times more massive than would be expected based on the best-fitting relationship from Reines & Volonteri (2015).

The lower host-galaxy stellar masses and higher SMBH masses of `TNG300` AGNs compared to those of Reines & Volonteri (2015) could be caused by several factors. For example, in `TNG300`, a SMBH of mass $6.2\times10^6\,M_\odot$ is seeded into any friends-of-friends halo whose mass exceeds $7.3\times10^{10}\,M_\odot$, which is based on the host–halo relationship of Di Matteo et al. (2008) and Sijacki et al. (2009). This initial mass could be too large, resulting in more massive SMBHs in `TNG300` by $z=0.0$. This would, however, also affect the relationships in the top panels of Figure 13. Another explanation could involve the AGN feedback models in `TNG300`, which describe how energy is injected into the galaxies and circumgalactic medium (CGM). Zinger et al. (2020) find the AGN feedback channel of `TNG300` AGNs to be both highly "ejective" and "preventative." This means the AGN state is highly efficient at expelling star-forming gas from the galaxy and increasing the entropy of the CGM, which strongly quenches future star formation within the galaxy. Therefore, if the feedback injection is over-tuned, or if `TNG300` galaxies spend too long in their "active" state, this could cause the host-galaxy stellar masses of `TNG300` AGNs to be lower than those of Reines & Volonteri (2015).

Our results for the systematic differences between void and nonvoid galaxies in the `TNG300` simulation are consistent with the expectation that the two populations of galaxies underwent somewhat different evolutionary paths, with nonvoid galaxies forming in regions of space that had both higher gas densities and higher galaxy densities than void galaxies. In a universe in which structure forms hierarchically, this naturally leads to

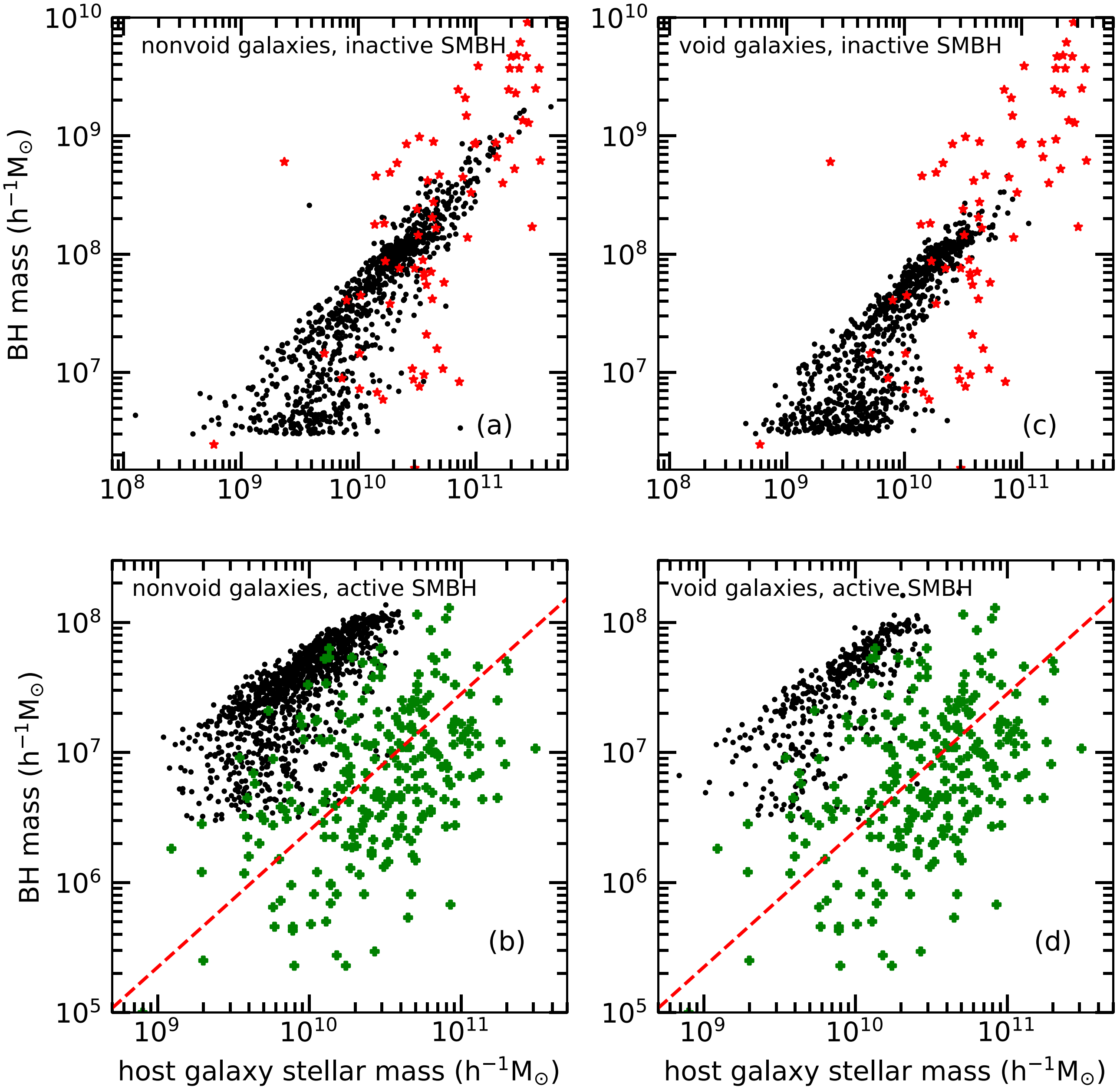

Figure 13. Black points: supermassive black hole (SMBH) mass vs. galaxy stellar mass in the `TNG300` simulation. Top: inactive SMBH. Bottom: active SMBH. Left: nonvoid galaxies. Right: void galaxies. Red stars and green crosses: observational results obtained by Reines & Volonteri (2015). Dashed red lines: best-fitting relationship between SMBH mass and galaxy stellar mass for observed galaxies with an AGN in Reines & Volonteri (2015). For clarity of the figure, randomly selected fractions of the `TNG300` data points are plotted (1% in panel (a), 10% in panel (b), 10% in panel (c), and 30% in panel (d)).

nonvoid galaxies forming earlier than void galaxies (i.e., due to biased galaxy formation in which the highest peaks collapse first) and becoming larger on average than void galaxies (i.e., due to both a larger local reservoir of gas and a higher frequency of galaxy collisions outside the voids). Here, we have investigated void and nonvoid galaxy properties in a single simulation snapshot (corresponding to the present epoch) and, therefore, we cannot make definitive statements about the degree to which the evolutionary paths of the `TNG300` void and nonvoid galaxies differed, and the ways in which those differences affected their physical properties at $z = 0$. Further work, concentrated on the details of the evolution of void and nonvoid galaxies over cosmic time, will be necessary to establish and quantify differences in the evolutionary paths and the resulting effects on the natures of the two populations of galaxies.

Acknowledgments

We are grateful to the anonymous reviewer for helpful comments and suggestions that improved the manuscript. This work was partially supported by National Science Foundation grant AST-2009397. The IllustrisTNG simulations were undertaken with compute time awarded by the Gauss Centre for Supercomputing (GCS) under GCS Large-Scale Projects GCS-ILLU and GCS-DWAR on the GCS share of the supercomputer Hazel Hen at the High Performance Computing Center Stuttgart (HLRS), as well as on the machines of the Max Planck Computing and Data Facility (MPCDF) in Garching, Germany. In addition, we are pleased to acknowledge that the computational work reported on in this paper was performed on the Shared Computing Cluster, which is administered by Boston University's Research Computing Services.

ORCID iDs

Olivia Curtis https://orcid.org/0000-0002-0212-4563
Bryanne McDonough https://orcid.org/0000-0001-6928-4345
Tereasa G. Brainerd https://orcid.org/0000-0001-7917-7623

References

Alam, S., Aubert, M., Avila, S., et al. 2021, PhRvD, 103, 083533
Alpaslan, M., Robotham, A. S. G., Obreschkow, D., et al. 2014, MNRAS, 440, L106
Amiri, A., Tavasoli, S., & De Zotti, G. 2019, ApJ, 874, 140
Argudo-Fernández, M., Lacerna, I., & Duarte Puertas, S. 2018, A&A, 620, A113
Astropy Collaboration, Price-Whelan, A. M., Sipőcz, B. M., et al. 2018, AJ, 156, 123
Astropy Collaboration, Robitaille, T. P., Tollerud, E. J., et al. 2013, A&A, 558, A33
Banerjee, A., & Dalal, N. 2016, JCAP, 2016, 015
Bermejo, R., Wilding, G., van de Weygaert, R., et al. 2022, arXiv:2206.14655
Bertschinger, E. 1998, ARA&A, 36, 599
Beygu, B., Kreckel, K., van der Hulst, J. M., et al. 2016, MNRAS, 458, 394
Blumenthal, G. R., da Costa, L. N., Goldwirth, D. S., Lecar, M., & Piran, T. 1992, ApJ, 388, 234
Bothun, G. D., Geller, M. J., Kurtz, M. J., Huchra, J. P., & Schild, R. E. 1992, ApJ, 395, 347
Brainerd, T. G. 2018, ApJL, 868, L7
Cai, Y.-C., Neyrinck, M., Mao, Q., et al. 2017, MNRAS, 466, 3364
Cai, Y.-C., Padilla, N., & Li, B. 2015, MNRAS, 451, 1036
Carter, B. J., Fabricant, D. G., Geller, M. J., Kurtz, M. J., & McLean, B. 2001, ApJ, 559, 606
Ceccarelli, L., Duplancic, F., & Garcia Lambas, D. 2022, MNRAS, 509, 1805
Clampitt, J., Cai, Y.-C., & Li, B. 2013, MNRAS, 431, 749
Constantin, A., Hoyle, F., & Vogeley, M. S. 2008, ApJ, 673, 715
Contarini, S., Marulli, F., Moscardini, L., et al. 2021, MNRAS, 504, 5021
Croton, D. J., Farrar, G. R., Norberg, P., et al. 2005, MNRAS, 356, 1155
Dark Energy Survey Collaboration, Abbott, T., Abdalla, F. B., et al. 2016, MNRAS, 460, 1270
Dávila-Kurbán, F., Lares, M., & Lambas, D. G. 2023, MNRAS, 518, 3095
Dawson, K. S., Schlegel, D. J., Ahn, C. P., et al. 2013, AJ, 145, 10
Di Matteo, T., Colberg, J., Springel, V., Hernquist, L., & Sijacki, D. 2008, ApJ, 676, 33
Dolag, K., Komatsu, E., & Sunyaev, R. 2016, MNRAS, 463, 1797
Domínguez-Gómez, J., Lisenfeld, U., Pérez, I., et al. 2022, A&A, 658, A124
Douglass, K. A., Smith, J. A., & Demina, R. 2019, ApJ, 886, 153
Douglass, K. A., & Vogeley, M. S. 2017, ApJ, 834, 186
Douglass, K. A., Vogeley, M. S., & Cen, R. 2018, ApJ, 864, 144
Dubois, Y., Peirani, S., Pichon, C., et al. 2016, MNRAS, 463, 3948
El-Ad, H., & Piran, T. 1997, ApJ, 491, 421
Falck, B., Koyama, K., Zhao, G.-B., & Cautun, M. 2018, MNRAS, 475, 3262
Flaugher, B. 2005, IJMPA, 20, 3121
Florez, J., Berlind, A. A., Kannappan, S. J., et al. 2021, ApJ, 906, 97
Genel, S., Vogelsberger, M., Springel, V., et al. 2014, MNRAS, 445, 175
Gibbons, G. W., Werner, M. C., Yoshida, N., & Chon, S. 2014, MNRAS, 438, 1603
Giovanelli, R., & Haynes, M. P. 1991, ARA&A, 29, 499
Goldberg, D. M., & Vogeley, M. S. 2004, ApJ, 605, 1
González Delgado, R. M., Pérez, E., Cid Fernandes, R., et al. 2014, A&A, 562, A47
Habouzit, M., Pisani, A., Goulding, A., et al. 2020, MNRAS, 493, 899
Hamaus, N., Pisani, A., Choi, J.-A., et al. 2020, JCAP, 2020, 023
Hamaus, N., Pisani, A., Sutter, P. M., et al. 2016, PhRvL, 117, 091302
Hirschmann, M., Dolag, K., Saro, A., et al. 2014, MNRAS, 442, 2304
Hoyle, F., & Vogeley, M. S. 2004, ApJ, 607, 751
Hoyle, F., Vogeley, M. S., & Pan, D. 2012, MNRAS, 426, 3041
Icke, V. 1984, MNRAS, 206, 1P
Karhunen, K., Kotilainen, J. K., Falomo, R., & Bettoni, D. 2014, MNRAS, 441, 1802
Kauffmann, G., White, S. D. M., Heckman, T. M., et al. 2004, MNRAS, 353, 713
Kreckel, K., Platen, E., Aragón-Calvo, M. A., et al. 2012, AJ, 144, 16
Kreisch, C. D., Pisani, A., Carbone, C., et al. 2019, MNRAS, 488, 4413
Lesgourgues, J., & Pastor, S. 2006, PhR, 429, 307
Li, B., Zhao, G.-B., & Koyama, K. 2012, MNRAS, 421, 3481
Li, H., Mao, S., Cappellari, M., et al. 2018, MNRAS, 476, 1765
Liddle, A. R., & Lyth, D. H. 1993, PhR, 231, 1
Liu, C.-X., Pan, D. C., Hao, L., et al. 2015, ApJ, 810, 165
Lopes, P. A. A., Ribeiro, A. L. B., & Rembold, S. B. 2017, MNRAS, 472, 409
Lu, S., Cappellari, M., Mao, S., Ge, J., & Li, R. 2020, MNRAS, 495, 4820
Manzer, L. H., & De Robertis, M. M. 2014, ApJ, 788, 140
Mao, Q., Berlind, A. A., Scherrer, R. J., et al. 2017, ApJ, 835, 161
Marinacci, F., Vogelsberger, M., Pakmor, R., et al. 2018, MNRAS, 480, 5113
Massara, E., Villaescusa-Navarro, F., Viel, M., & Sutter, P. M. 2015, JCAP, 2015, 018
McDonough, B., & Brainerd, T. G. 2022, ApJ, 933, 161
Mishra, H. D., Dai, X., & Guerras, E. 2021, ApJL, 922, L17
Moorman, C. M., Vogeley, M. S., Hoyle, F., et al. 2014, MNRAS, 444, 3559
Nadathur, S., Carter, P. M., Percival, W. J., Winther, H. A., & Bautista, J. E. 2019, PhRvD, 100, 023504
Naiman, J. P., Pillepich, A., Springel, V., et al. 2018, MNRAS, 477, 1206
Nelson, D., Pillepich, A., Springel, V., et al. 2018, MNRAS, 475, 624
Neyrinck, M. C. 2008, MNRAS, 386, 2101
Padilla, N. D., Ceccarelli, L., & Lambas, D. G. 2005, MNRAS, 363, 977
Paillas, E., Cautun, M., Li, B., et al. 2019, MNRAS, 484, 1149
Paillas, E., Lagos, C. D. P., Padilla, N., et al. 2017, MNRAS, 470, 4434
Pandey, D., Saha, K., & Pradhan, A. C. 2021, ApJ, 919, 101
Patiri, S. G., Prada, F., Holtzman, J., Klypin, A., & Betancort-Rijo, J. 2006, MNRAS, 372, 1710
Peebles, P. J. E. 2001, ApJ, 557, 495
Pillepich, A., Nelson, D., Hernquist, L., et al. 2018, MNRAS, 475, 648
Planck Collaboration, Ade, P. A. R., Aghanim, N., et al. 2016, A&A, 594, A13
Planck Collaboration, Aghanim, N., Akrami, Y., et al. 2020, A&A, 641, A1
Platen, E. 2009, PhD thesis, Univ. Groningen, Netherlands
Platen, E., van de Weygaert, R., & Jones, B. J. T. 2007, MNRAS, 380, 551
Pollina, G., Baldi, M., Marulli, F., & Moscardini, L. 2016, MNRAS, 455, 3075
Pollina, G., Hamaus, N., Dolag, K., et al. 2017, MNRAS, 469, 787
Reines, A. E., & Volonteri, M. 2015, ApJ, 813, 82
Ricciardelli, E., Quilis, V., & Varela, J. 2014, MNRAS, 440, 601
Rodríguez Medrano, A. M., Paz, D. J., Stasyszyn, F. A., & Ruiz, A. N. 2022, MNRAS, 511, 2688
Rojas, R. R., Vogeley, M. S., Hoyle, F., & Brinkmann, J. 2004, ApJ, 617, 50
Rosas-Guevara, Y., Tissera, P., Lagos, C. d. P, Paillas, E., & Padilla, N. 2022, MNRAS, 517, 712
Ruiz, A. N., Paz, D. J., Lares, M., et al. 2015, MNRAS, 448, 1471
Sabater, J., Best, P. N., & Heckman, T. M. 2015, MNRAS, 447, 110
Sánchez, C., Clampitt, J., Kovacs, A., et al. 2017, MNRAS, 465, 746
Schaye, J., Crain, R. A., Bower, R. G., et al. 2015, MNRAS, 446, 521
Schechter, P. 1976, ApJ, 203, 297
Schuster, N., Hamaus, N., Dolag, K., & Weller, J. 2023, JCAP, 2023, 031
Schuster, N., Hamaus, N., Pisani, A., et al. 2019, JCAP, 2019, 055
Scott, N., Brough, S., Croom, S. M., et al. 2017, MNRAS, 472, 2833
Sheth, R. K., & van de Weygaert, R. 2004, MNRAS, 350, 517
Sijacki, D., Springel, V., & Haehnelt, M. G. 2009, MNRAS, 400, 100
Sijacki, D., Vogelsberger, M., Genel, S., et al. 2015, MNRAS, 452, 575
Springel, V., Pakmor, R., Pillepich, A., et al. 2018, MNRAS, 475, 676
Sutter, P. M., Pisani, A., Wandelt, B. D., & Weinberg, D. H. 2014, MNRAS, 443, 2983
Szomoru, A., van Gorkom, J. H., Gregg, M. D., & Strauss, M. A. 1996, AJ, 111, 2150
Vallés-Pérez, D., Quilis, V., & Planelles, S. 2021, ApJL, 920, L2
van de Weygaert, R. 2016, in IAU Symp. 308, The Zeldovich Universe: Genesis and Growth of the Cosmic Web, ed. R. van de Weygaert et al. (Cambridge: Cambridge Univ. Press), 493
van de Weygaert, R., & van Kampen, E. 1993, MNRAS, 263, 481
Villaescusa-Navarro, F., Vogelsberger, M., Viel, M., & Loeb, A. 2013, MNRAS, 431, 3670
Vogelsberger, M., Genel, S., Springel, V., et al. 2014a, Natur, 509, 177
Vogelsberger, M., Genel, S., Springel, V., et al. 2014b, MNRAS, 444, 1518
Wegner, G. A., Salzer, J. J., Taylor, J. M., & Hirschauer, A. S. 2019, ApJ, 883, 29
Weinberger, R., Springel, V., Hernquist, L., et al. 2017, MNRAS, 465, 3291
Woodfinden, A., Nadathur, S., Percival, W. J., et al. 2022, MNRAS, 516, 4307
York, D. G., Adelman, J., Anderson, J. E., Jr., et al. 2000, AJ, 120, 1579
Zinger, E., Pillepich, A., Nelson, D., et al. 2020, MNRAS, 499, 768